

Effects of Inlet Distortion on the Flow Field in a Transonic Compressor Rotor

C. Hah

NASA Lewis Research Center,
Cleveland, OH 44135

D. C. Rabe

Wright-Patterson AFB,
Dayton, OH 45433

T. J. Sullivan

A. R. Wadia

GE Aircraft Engines,
Cincinnati, OH 45215

The effects of circumferential distortions in inlet total pressure on the flow field in a low-aspect-ratio, high-speed, high-pressure-ratio, transonic compressor rotor are investigated in this paper. The flow field was studied experimentally and numerically with and without inlet total pressure distortion. Total pressure distortion was created by screens mounted upstream from the rotor inlet. Circumferential distortions of eight periods per revolution were investigated at two different rotor speeds. The unsteady blade surface pressures were measured with miniature pressure transducers mounted in the blade. The flow fields with and without inlet total pressure distortion were analyzed numerically by solving steady and unsteady forms of the Reynolds-averaged Navier-Stokes equations. Steady three-dimensional viscous flow calculations were performed for the flow without inlet distortion while unsteady three-dimensional viscous flow calculations were used for the flow with inlet distortion. For the time-accurate calculation, circumferential and radial variations of the inlet total pressure were used as a time-dependent inflow boundary condition. A second-order implicit scheme was used for the time integration. The experimental measurements and the numerical analysis are highly complementary for this study because of the extreme complexity of the flow field. The current investigation shows that inlet flow distortions travel through the rotor blade passage and are convected into the following stator. At a high rotor speed where the flow is transonic, the passage shock was found to oscillate by as much as 20 percent of the blade chord, and very strong interactions between the unsteady passage shock and the blade boundary layer were observed. This interaction increases the effective blockage of the passage, resulting in an increased aerodynamic loss and a reduced stall margin. The strong interaction between the passage shock and the blade boundary layer increases the peak aerodynamic loss by about one percent.

Introduction

The design technology of transonic compressors has recently been significantly advanced. The combination of advanced non-intrusive measurement techniques and computational modeling methods has contributed substantially to understanding the detailed flow physics required to further advance transonic compressor design. Knowledge of the compressor response to non-uniform conditions of incoming flow is required for both civilian and military applications. Certain inflow distortions may cause blade vibrations at natural frequencies. Any failure of the vibrating airfoils can lead to catastrophic damage to the entire engine.

Various analytical studies have been reported that study the effects of inlet flow distortion on transonic compressor fields. Horlock (1968) provides some insights into the prediction of the change in aerodynamic loading. Other experimental studies measured aerodynamic performance under the influence of inlet flow distortion. Monsarrat (1969) measured the performance of a highly loaded transonic compressor stage with an inlet total pressure distortion. Bowditch and Coltrin (1983) and Longley (1988) performed experimental investigations on the effects of inlet distortion on compressor stability. Recently Rabe et al. (1995) used miniature high-response pressure transducers mounted on the rotor blade to study blade response to the inlet total pressure distortion in a state-of-the-art transonic compressor. Over the last decade, numerical techniques for the analysis

of turbomachinery flows have progressed significantly (Davis et al., 1988; Dawes, 1986; Denton, 1986; Giles, 1988; Hah, 1984; Moore and Moore, 1981; Rao and Delaney, 1990; etc.). Three-dimensional steady flow calculations based on the Reynolds-averaged Navier-Stokes equations are now relatively well established and routinely used to optimize blading and flow-path contours. At the present time, numerical methods do not always predict the absolute aerodynamic loss exactly because of the inadequate physical models. However, the variations of aerodynamic performance due to design changes are predicted adequately for engineering guidance. As numerical methods for the analysis of isolated blade rows have become mature, more studies have been made to study multistage flow phenomena with steady and unsteady methods (Adamczyk et al., 1986; Copenhaver et al., 1993; Denton and Singh, 1979; Giles, 1988; Gundy-Burlet et al., 1991; Hah et al., 1993; Jorgenson and Chima, 1988; Ni and Bogoian, 1989; Rai, 1985; Rao and Delaney, 1990; etc.). Although various numerical procedures have been developed to study blade row interactions in turbomachinery, very few attempts have been reported to investigate other important unsteady flow phenomena in multistage compressors (Smith, 1966; Mikolajczyk, 1977; Greitzer et al., 1994). For instance, very few numerical studies have been reported in the open literature that address the effects of inlet flow distortion on the time-dependent flow field in a transonic compressor. Hall et al. (1996) conducted a numerical study on the effects of inlet distortions on endwall treated fan rotors.

The present paper describes a study to advance our current understanding of the flow structure in a low-aspect-ratio, high-speed, high-pressure-ratio, transonic compressor rotor with inlet flow distortions. The experimental technique and the numerical

Contributed by the International Gas Turbine Institute and presented at the 41st International Gas Turbine and Aeroengine Congress and Exhibition, Birmingham, United Kingdom, June 10–13, 1996. Manuscript received at ASME Headquarters February 1996. Paper No. 96-GT-547. Associate Technical Editor: J. N. Shinn.

Table 1 Design parameters of the first-stage rotor

Parameter	Value
Rotor 1 Aspect Ratio	1.0
Rotor Tip Radius, cm(ft)	35.24(1.16)
Inlet Radius Ratio	0.33
Tip Solidity	1.50
Max. Thickness/Chord(Tip)	0.028
Number of Blades	16
Tip Speed, m/s(ft/s)	490.4(1609)
Rotor 1 Total Pressure Ratio	2.5
Corrected Design Flow, Kg/s(lbm/s)	71.95(158.6)

approach are used in a complementary way to understand the flow physics and provide confidence in the numerical and experimental results.

Motivation and Scope of the Paper

The objective of the current study is to advance our present understanding of the flow phenomena inside a low-aspect-ratio, high-speed, high-pressure-ratio, transonic compressor rotor subject to a circumferential total pressure distortion at the inlet. Although the gross effects of inflow distortion, such as airfoil vibration and compressor blade failure, are well known, the detailed flow mechanisms responsible for these effects are not well understood.

Flow measurements inside a transonic compressor rotor are extremely difficult to obtain even with the latest developments in measurement technique. Time-dependent flow field measurements in a transonic compressor rotor challenge the existing nonintrusive measurement techniques. For the present investigation, miniature high-response pressure transducers are mounted on the rotating blade as well as on the endwall. Such time-dependent pressure measurements on the blade in a high-speed machine have not previously been performed.

Because the present measurement techniques do not provide sufficient information to fully describe the unsteady flow phenomena inside the rotor, unsteady Navier-Stokes analyses are also performed. As is well known, currently available numerical meth-

ods based on the Reynolds-averaged Navier-Stokes equations do not always predict absolute values of the aerodynamic loss in turbomachinery. However, it is widely accepted that most important flow phenomena are properly captured with the current numerical methods. Therefore, the unsteady Reynolds-averaged Navier-Stokes equations are numerically solved to understand the flow phenomena inside the present transonic compressor when the inflow has a circumferential flow distortion.

For the current study, an inlet distortion pattern, which has eight distortion cells per revolution, is investigated at two rotor speeds. This distortion pattern has been selected for the convenience of analysis. However, we feel that the fundamental flow mechanisms found from the current study are valid for other type of distortion patterns (one or two distortion cells per revolution).

The present study shows that the experimental and the numerical methods are highly complementary in understanding such a complex flow structure because neither method alone explains the necessary flow physics. The results from the numerical analysis are compared with the available experimental data for both uniform inflow and nonuniform inflow conditions.

Test Rotor and Data Acquisition

The rotor investigated in this work is the first-stage rotor of a two-stage axial flow compressor. This rotor is an advanced state-of-the-art design consisting of 16 low-aspect-ratio blades similar to those described by Wennerstrom (1984). Table 1 provides a summary of the design performance of this rotor. Figure 1 presents a cross section of the test configuration used to evaluate the rotor performance. Overall performance of the rotor was calculated from measured total pressure and temperature values at the rotor inlet and exit.

Inlet total pressure distortion was created by screens located approximately 102 cm upstream of the hub leading edge of rotor 1. Measurement of the compressor inlet pressure profile with or without inlet distortion was performed at the distortion measurement plane. Both of these locations are shown in Fig. 1. The distortion plane steady-state total pressure measurements were obtained using eight rakes. Each rake was equally spaced circumferentially, and each had five radially distributed pressure measurements. These inlet total pressure measurements were weighted by the flow area they measured to obtain an area averaged overall inlet total pressure. The inlet total temperature was measured by 49 thermocouples located at a measurement plane farther upstream than the distortion screen location shown in Fig. 1. Since these probes were placed to measure essentially equal areas of the inlet flow, a simple average of their measurements represents an area-averaged value of inlet total tempera-

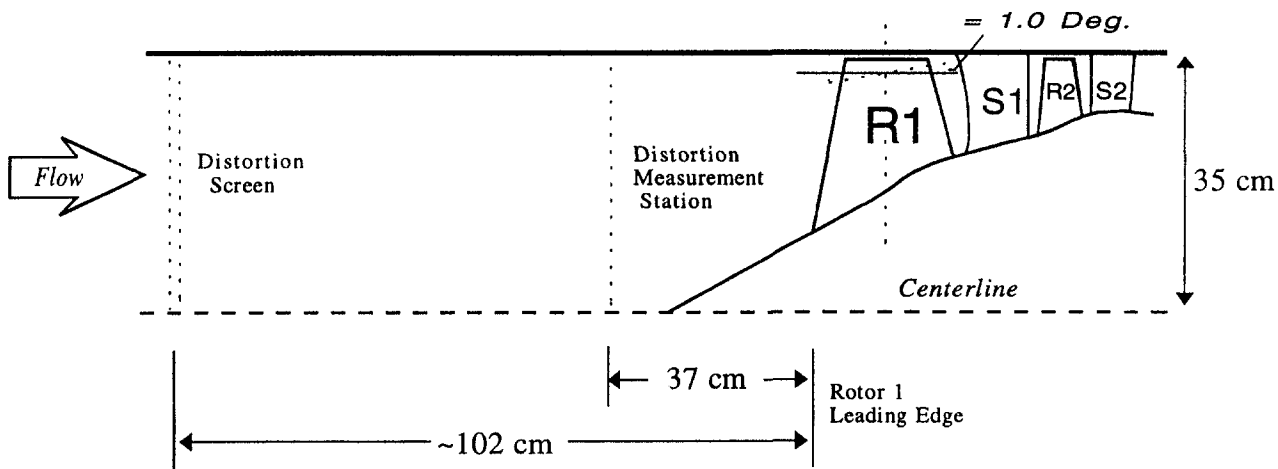


Fig. 1 Test compressor and generation of distortion

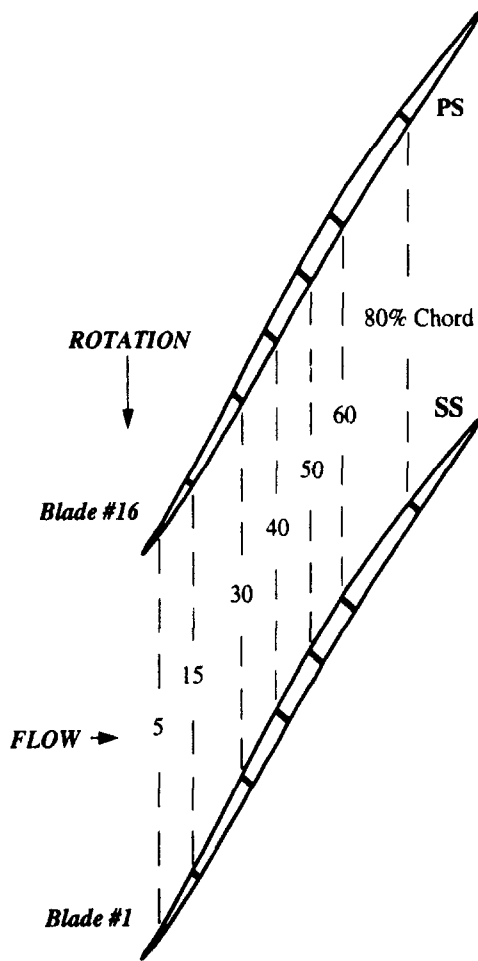


Fig. 2 Blade-mounted transducer configuration

ture. This temperature was considered to be constant and uniform from that measurement station to the compressor inlet in all test conditions.

Rotor exit total pressure and temperature measurements were made using steady-state probes located on the leading edge of the first stage stator (S1) in Fig. 1. Three of the 41 stators, approximately equally spaced circumferentially, were instrumented at seven radial locations. These measurements were area-averaged to obtain the overall rotor exit total pressure and temperature. With these measurements at the rotor inlet and exit, overall performance could be calculated.

With a distorted inlet test condition, the exit total temperature profile and inlet and exit total pressure profiles were enhanced by rotating the distortion screen to 10 different positions within one period of the distortion pattern. At each screen position, the inlet and exit total pressure and temperature measurements were acquired. This resulted in 400 inlet total pressure measurements and 210 exit total pressure and exit total temperature measurements. These measurements were area-averaged to quantify the rotor inlet total pressure and the rotor exit total pressure and temperature with distortion. Overall mass flow was measured by a venturi located approximately 30 m downstream from the compressor.

Additional measurements of the unsteady rotor blade surface pressure and end-wall pressure provided detailed measurements for comparison with computational results. The blade surface pressure measurements were obtained using two sets of seven pressure transducers that were embedded in two adjacent blades of the first-stage rotor, as shown in Fig. 2. These transducers were located along a line representing a stream line used in the

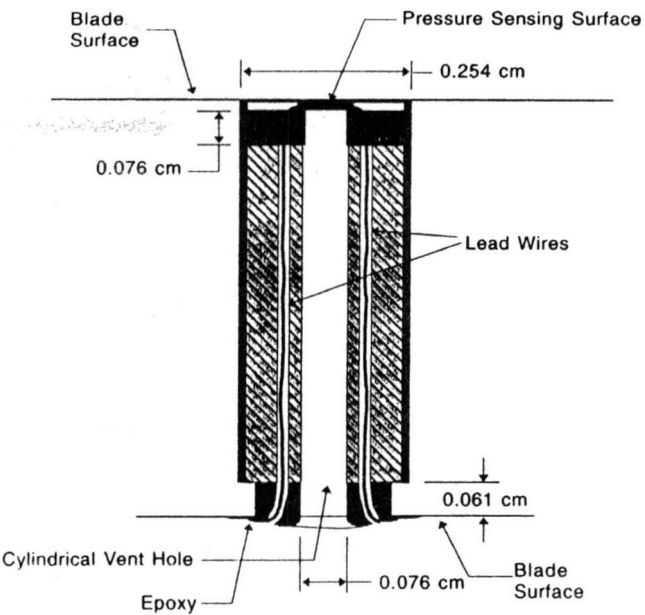


Fig. 3 Blade-mounted transducer installation

initial rotor design. This resulted in the transducers being at an angle of one degree to the rotor centerline as shown in Fig. 1. The mounting of the transducers is shown schematically in Fig. 3. As seen in this figure, one surface of the pressure transducer is essentially flush with the blade surface while the reference side of the pressure transducer is at the end of a reference hole. For all of the transducer mounting configurations, the length of this hole permitted a natural frequency of 20 kHz or higher. These transducers were installed in the blade such that the sensing surface was essentially flush on the surface of the blade facing the accompanying instrumented blade. The axial positions of these transducers are shown in Fig. 2. This configuration resulted in redundancy of the unsteady differential surface pressure measurement at each chord location that provided data

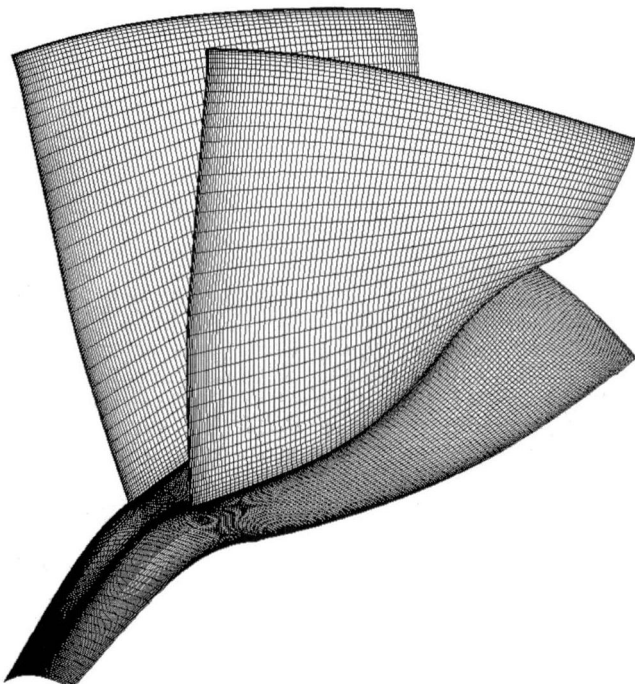


Fig. 4 Computational grid

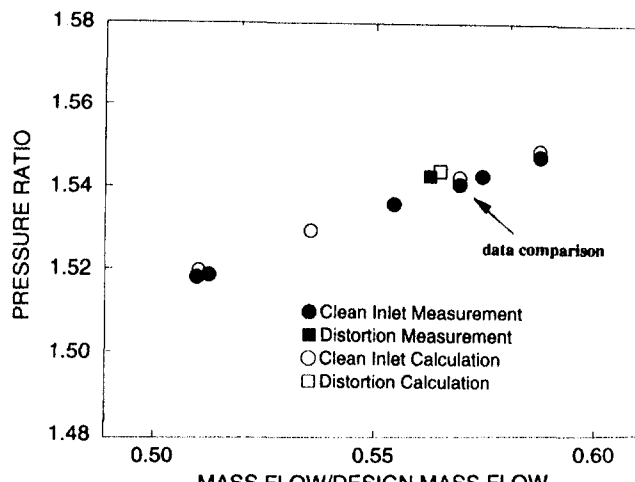


Fig. 5(a) Rotor speed line at 68 percent speed

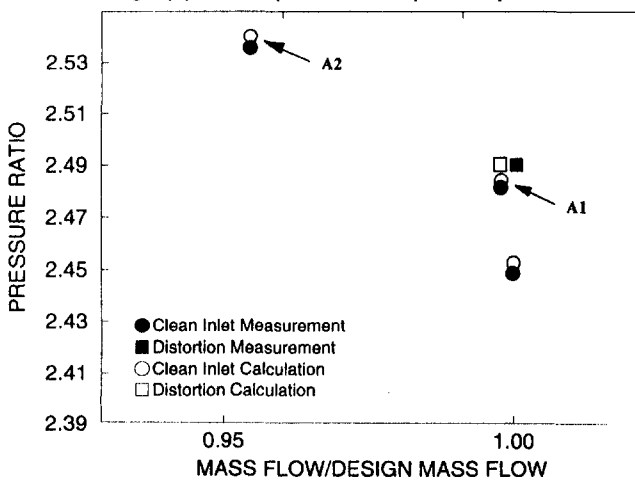


Fig. 5(b) Rotor speed line at 98 percent speed

validation and became beneficial with transducer attrition during the test. During data acquisition of the blade surface pressure measurements, the eight inlet rakes located at the distortion plane in Fig. 1 were removed so the only distortion present in the flow resulted from the distortion screen. These measurements were then compared to the unsteady results of the computational analysis.

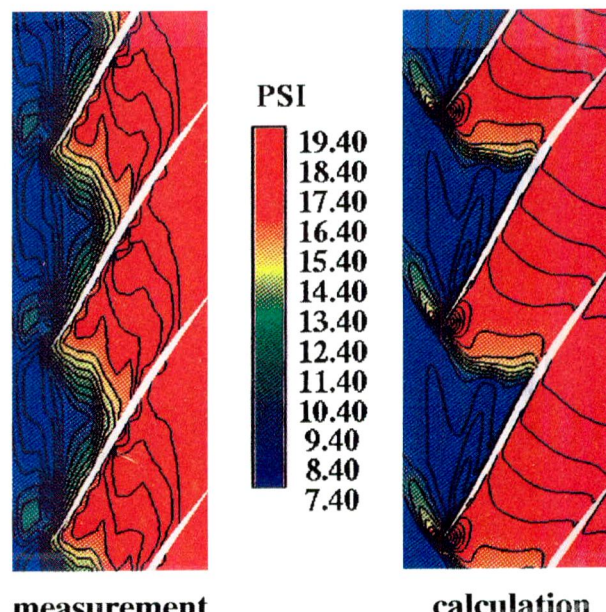
The case-mounted high response pressure transducers also provided detailed flow measurements that could be used for validation of the numerical analysis. Sixteen of these transducers were located over the first-stage rotor blade. The data obtained from these measurements were processed as described by Russler (1995). These measurements were only acquired with a clean inlet condition. These measurements were then used to provide a detailed representation of the blade passage flow field that was compared to the computational results.

Accuracy of the measurements was maintained such that the temperatures were accurate to $\pm 0.17^\circ\text{C}$, the inlet steady-state pressure measurements were accurate to $\pm 0.002 \text{ atm}$, and the stator 1 pressure measurements were accurate to $\pm 0.007 \text{ atm}$. This resulted in an uncertainty of 0.8 percent in pressure ratio and 0.1 percent in temperature ratio. This accuracy does not consider the uncertainty due to averaging discrete pressures to determine the measurement plane average. The mass flow accuracy was considered to be ± 0.5 percent at design flow. The unsteady differential pressure measurements on the blade were considered accurate to $\pm 0.031 \text{ atm}$, which is approximately equal to the maximum pressure recorded by these pressure transducers. The high response pressure measurements on the case

endwall were considered accurate to $\pm 0.031 \text{ atm}$ or 2.3 percent of the maximum exit static pressure measured during the test. All of these measurements were averaged to reduce the effect of noise or scatter on the measurement. The steady-state pressure and temperature values consisted of an average of 30 individual measurements. The case pressures were ensemble-averaged over at least 100 revolutions of a specific blade passage. The blade pressure measurements were ensemble-averaged from at least 1200 periods of distortion.

Numerical Method

Two types of numerical analysis were performed for the current study. A steady three-dimensional Navier-Stokes analysis was applied to the rotor flow field with the clean inflow condition. The detailed numerical procedures for the steady flow analysis were previously reported (Hah, 1987; Hah and Wennerstrom, 1990). With a circumferentially nonuniform distribution of inlet flow conditions, the compressor flow field becomes time dependent. To capture proper physics inside the blade passage, an unsteady, three-dimensional, viscous flow analysis was used for the flow with inlet distortions. For a time-periodic inflow condition, any instantaneous flow variable can be split



measurement

calculation

Fig. 6(a) Shroud static pressure distribution near peak efficiency

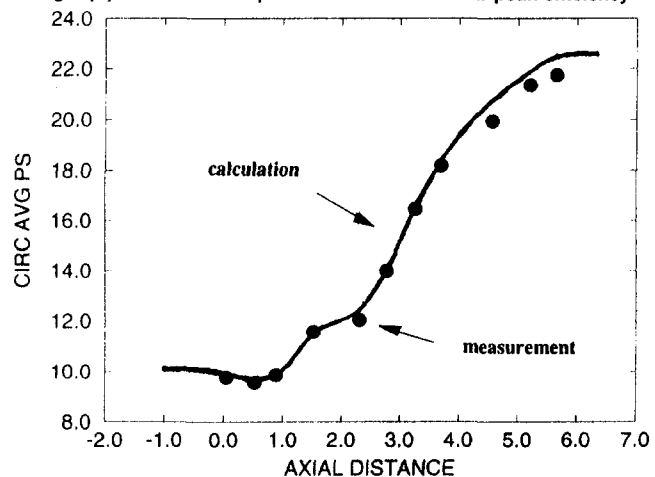


Fig. 6(b) Comparison of static pressure rise on the endwall

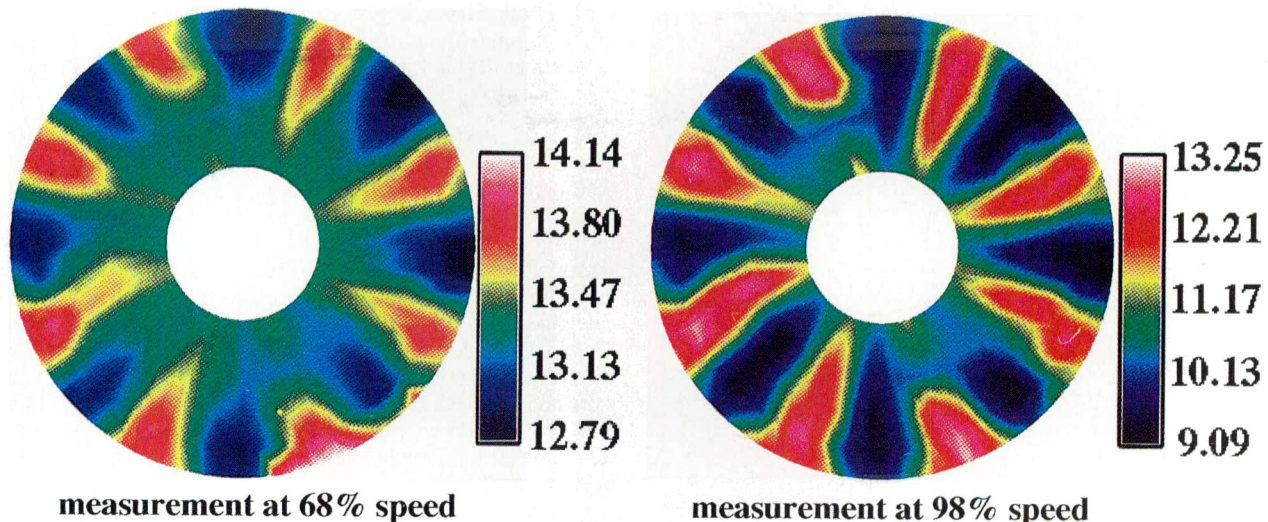


Fig. 7 Total pressure distributions at inlet

into three components; the time-averaged component, the periodic fluctuation due to the inlet flow distortion, and the turbulent fluctuation. The sum of the first two parts is the phase-averaged value, which is a function of time and space. The present study aims to solve numerically for this ensemble-averaged flow field. The effects of the turbulent fluctuations are included through the turbulence model. The turbulence is represented by the ensemble-averaged turbulence kinetic energy and the turbulence dissipation rate. These two turbulence variables are obtained by solving unsteady semi-empirical transport equations.

A three-dimensional steady Navier-Stokes code, which has been successfully tested for a wide range of turbomachinery flows (Hah, 1984, 1987), was extended to execute the time-accurate calculations. Previous studies (Cho et al., 1993; Hah et al., 1993) have shown that high-order discretization schemes are necessary in both space and time to avoid excessive numerical dissipation. For the time-dependent terms, an implicit second-order scheme is used. For unsteady flow calculations, the size of the time step is primarily determined by the requirement for physical accuracy. However, the time step is also restricted

by the numerical stability. For the current implicit time integration approach, a subiteration is performed at each time step. The computational grid is shown in Fig. 4. The grid consists of 100 nodes in the blade-to-blade direction, 46 nodes in the spanwise direction, and 152 nodes in the streamwise direction. Six nodes in the spanwise direction are used to describe the tip clearance region. With eight inlet distortion cells per revolution, two rotor blade passages encompass one period of the inlet distortion. Therefore, flows in two rotor blade passages shown in Fig. 4 were solved numerically. The numerical solution is advanced in time such that the two blade passages traverse one distortion pattern in 100 time steps. This corresponds to an actual time step of 0.0000057 s. Between 10 and 20 subiterations are necessary at each time step to reduce the residual below an acceptable value.

At each time step, the governing equations are solved with an implicit relaxation method using a fully conservative control volume approach. A third-order accurate interpolation scheme is used for the discretization of the convection terms and central differencing is used for the diffusion terms. The method is of

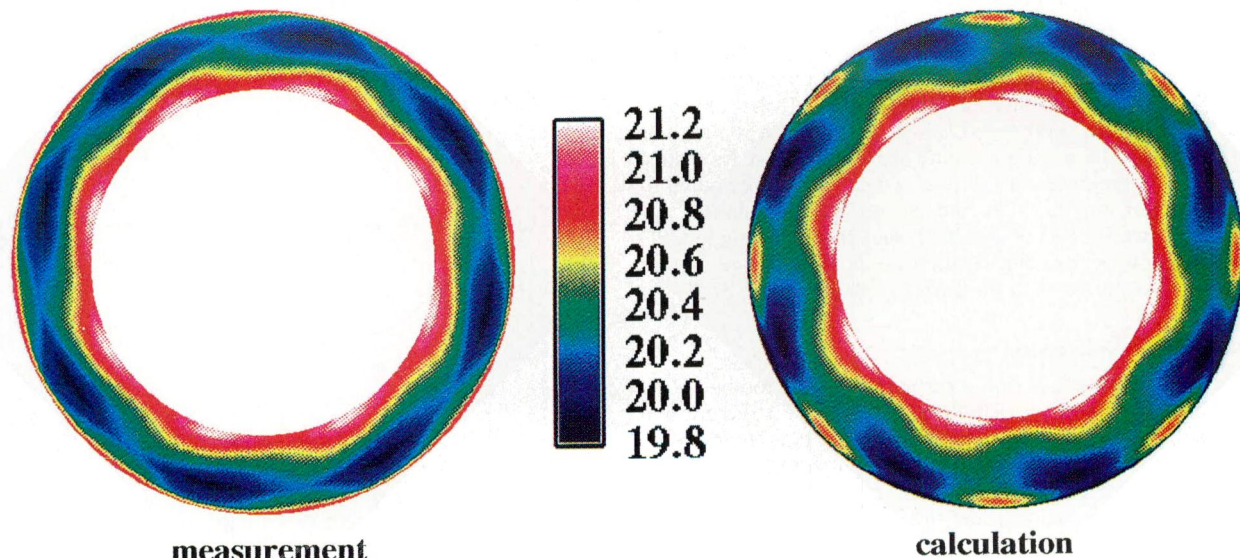


Fig. 8 Comparison of total pressure distributions at exit for 68 percent rotor speed

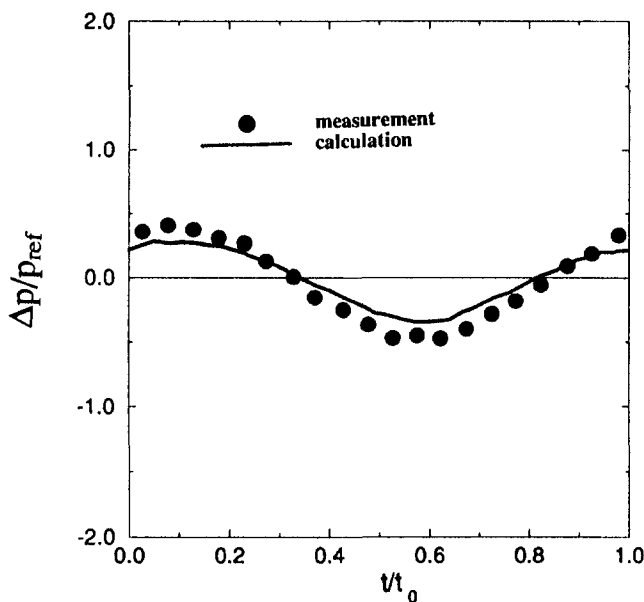


Fig. 9 Transient static pressure difference at 80 percent chord for 68 percent rotor speed

second-order accuracy with smoothly varying grids. At the inlet of the computational domain, instantaneous values of the total pressure that correspond to the distortion pattern are specified along with the total temperature. Also, two velocity components are specified at the inlet. No unsteady measurements of static pressure or other flow variables are available downstream of the rotor. Therefore, static pressure was prescribed at one circumferential location on the shroud at the outlet of the computational domain. Nonreflective procedures are used at the exit to minimize the influence of upstream effects. Residuals of each finite difference equation are integrated over the entire flow domain at each subiteration. When the integrated residuals of all the equations are reduced by four orders of magnitude from their initial values during the subiteration, the solution is advanced to the next time step. Further details of the computational procedures for the unsteady flow analysis are given by Hah et al. (1993) and Gallus et al. (1995). A steady solution is first obtained, and the converged steady solution is used as a starting condition for the unsteady calculations. Variations of mass flow rate and rotor efficiency were monitored to determine the convergence. When these quantities became periodic, the solution was assumed to be converged. A relatively large number of computational cycles is required to reach a periodic unsteady solution because of vortex shedding inside the rotor passage. For the lower rotor speed, about twelve distortion periods were calculated to reach a periodic state. About twenty distortion periods were necessary to obtain a converged periodic unsteady solution for the high rotor speed. The calculation was executed on a CRAY C-90 computer and about one single-CPU hour was required to advance the time-accurate solution over one distortion period with the current computational grid.

Results and Discussion

The primary objective of the current study was to investigate the effects of inlet flow distortion on the flow structure and the aerodynamic performance of a low-aspect-ratio, high-speed, transonic axial flow compressor. The computational results were compared to experimental data when appropriate to gain confidence in the computational and the experimental results. This comparison was first performed with the clean inlet flow condition to obtain the overall performance of rotor 1 and the detailed flow structure near the casing. Then, comparisons were made

for the flow with inlet distortion. After establishing confidence in the computational results, the numerical results were used to understand detailed flow structures that are responsible for the changes in aerodynamic performance of the rotor.

Overall Performance and Shock Structure With Clean Inlet

The design pressure ratio and mass flow occurred at 98.6 percent of the intended design speed of 13,288 rpm. The tip speed of the rotor at 98.6 percent speed was 483.5 m/s resulting in a blade tip Mach number of 1.7. The compressor was also tested at 98 and 68 percent rotor design speed with and without an inlet total pressure distortion. The measured and calculated pressure rise characteristics of the rotor are given in Fig. 5. The calculated performance of the rotor with the inlet distortion was obtained by area-averaging instantaneous values over one periodic cycle similar to the experimental technique.

When a blade encounters a low total pressure region of the distortion pattern, the blade loading increases because the blade operates with the same exit static pressure. Therefore, the effective blockage inside the rotor passage increases and the rotor operates closer to the stall condition. To study the effects of the inflow distortion on the blade efficiency, the flow with the inlet distortion at 98 percent speed is compared with a clean inlet flow, which has a distribution of blade loading similar to that of the distortion case, and to the clean inlet flow with the initial blade loading. Altogether, measured flow fields at four operating conditions and calculated flow fields at five conditions are investigated in detail. The four measured and five calculated flow conditions are marked in Fig. 5. The total pressure ratios in Fig. 5 were obtained by area-averaging for both the measurement and the calculation. The results in Fig. 5 indicate that the numerical solution calculates a slightly higher pressure rise than the measured value, both with a clean inlet and with an inlet distortion. However, the overall trend is very well represented by the calculation.

In Fig. 6, measured and calculated endwall shock structures and the static pressure rise across the rotor near peak efficiency with clean inlet at 98 percent rotor speed are compared. The numerical results show a stronger interaction between the tip clearance vortex and the passage shock than the measurements near the entrance of the rotor passage. Similar flow interactions inside the tip clearance region were previously observed in a high-speed compressor rotor (Copenhaver et al., 1993; Hah and

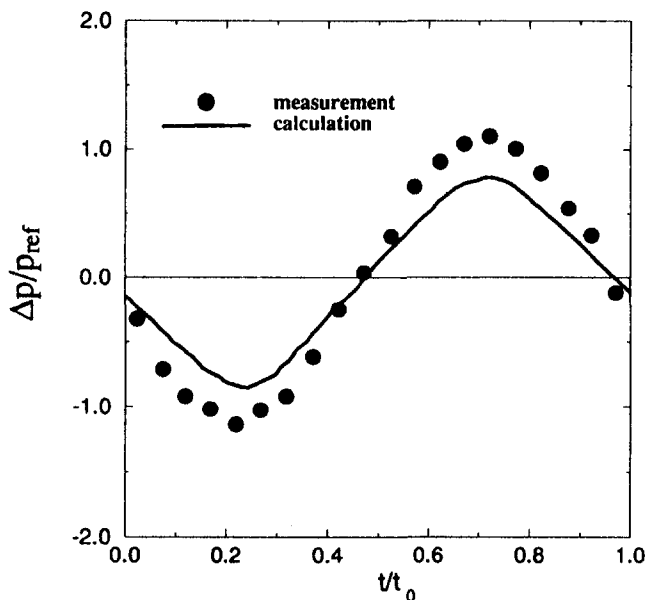


Fig. 10 Transient static pressure difference at 80 percent chord for 98 percent rotor speed

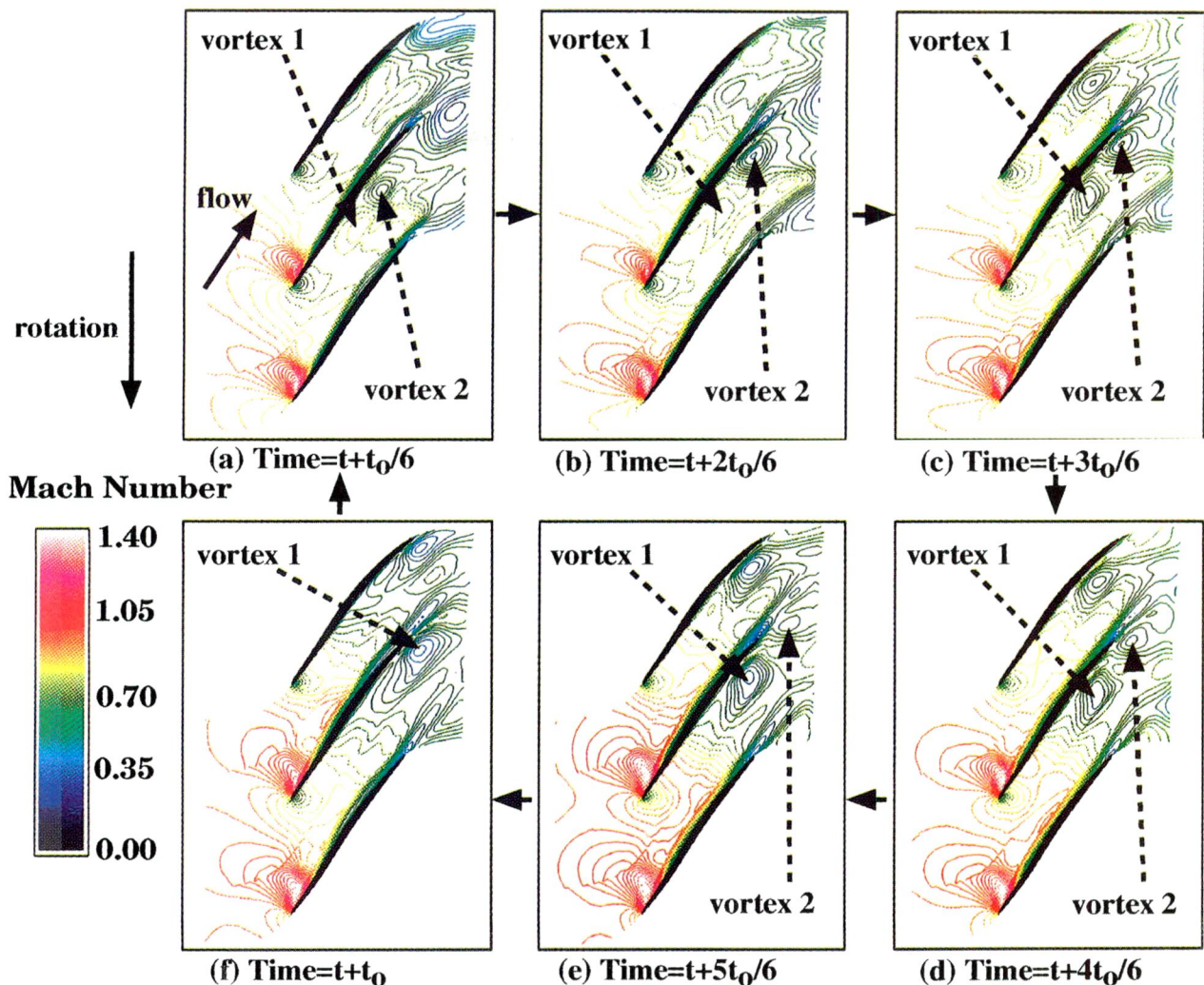


Fig. 11 Instantaneous Mach number contours at 85 percent span for 68 percent rotor speed

Wennerstrom, 1990). The limited number of pressure transducers mounted on the endwall limits the resolution of the flow field. Reasonably good agreements between the measurements and the calculation shown in Figs. 5 and 6 indicate that overall flow structures in the present high-pressure ratio compressor rotor are properly modeled by the current numerical procedure.

Flow Fields With Inlet Total Pressure Distortion. Inlet total pressure distortion patterns were created with an eight per revolution screen in the experimental study (Russler, 1994). The test conditions were selected to provide forcing functions to evaluate the rotor at resonance conditions. For the present work, effects of inlet distortion on the rotor flow field are studied in detail at two rotor speeds. In the following sections, the changes in distortion pattern through the rotor and transient static pressure at 85 percent span are first compared between the measurement and the calculation. Then, detailed flow characteristics in the rotor passage with the inlet distortion are examined with the numerical solution.

Distortion Pattern and Transient Blade Static Pressure. The measured distributions of inlet total pressure are shown in Fig. 7 at two test conditions. As shown in Fig. 7, each distribution has eight nearly sinusoidal profiles per revolution. The average maximum and minimum values of the total pressure for the eight periods are 12.86 psi and 9.27 psi for the high rotor speed. Corresponding values for the low rotor speed are

13.96 psi and 12.93 psi. The change in total pressure across the distortion is more than three times larger at high rotor speed than that at low speed. However, the relative magnitude of the total pressure change to the inlet dynamic head is about the same for the two speeds. For numerical analyses, the eight profiles at each rotor speed are averaged and eight identical distortion patterns per revolution are assumed. These averaged profiles, which are slightly asymmetric, are used as the inflow boundary conditions for the unsteady flow calculations.

In Fig. 8, total pressure distributions at the exit of the rotor are compared between the measurement and the calculation at 68 percent rotor design speed. The total pressure distributions shown in Fig. 8 are in the stationary frame, and the distributions are due to the nonuniform distribution upstream of the rotor. These total pressure profiles are convected to the following stator. The measurements show that the inlet distortion patterns are not mixed out completely by the rotor. The numerical results agree well with the measurements. The numerical values in Fig. 8 were obtained by averaging 100 instantaneous values through one distortion cycle after the periodic unsteady solution was obtained. A region with high total pressure near the hub and a region with low total pressure near 60–70 percent of the span are both observed from the measurement as well as from the calculation. Near the shroud, both high total pressure and low total pressure regions are shown. The distribution of total pressure near the shroud may be due to the interaction of the incom-

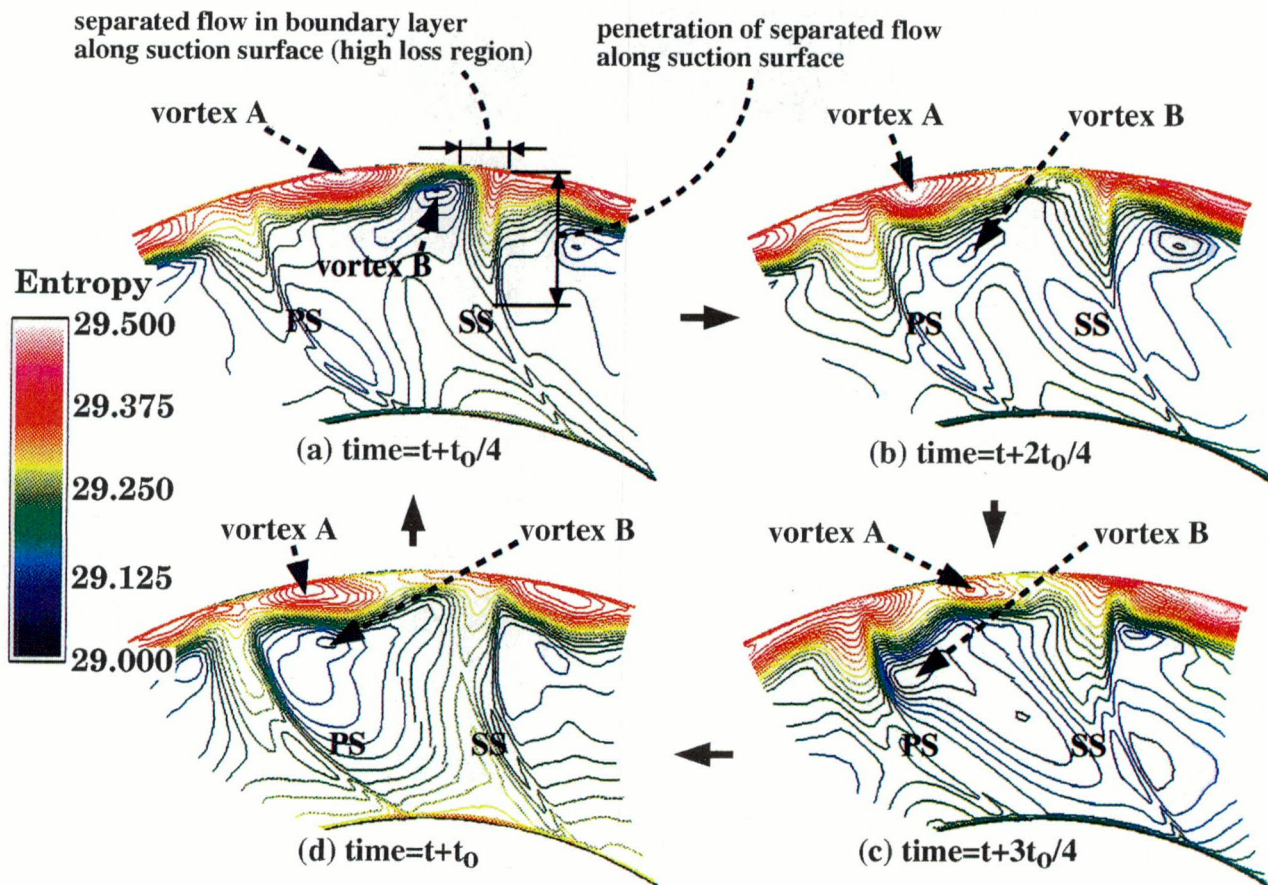


Fig. 12 Instantaneous entropy contours at 5 percent chord downstream of trailing edge for 68 percent rotor speed

ing distortion pattern with the tip clearance vortex. The results in Figs. 7 and 8 show that the total pressure distortion pattern travels through the rotor passage. The distortion pattern changes its shape substantially. However, eight distinctive distortion cells are present at the exit of the rotor.

Transient static pressure profiles at 80 percent blade chord and at 85 percent span are compared between the measurements and the calculation in Figs. 9 and 10. The values in Figs. 9 and 10 are the transient difference between the static pressures on the suction and the pressure sides of the blade for one period of distortion. The numerical profiles agree fairly well with the measured values. However, the calculated peak-to-peak variation is smaller than that measured at both rotor speeds. For the current numerical analysis, it is assumed that the geometric deflection of rotor blades does not change during rotation. The change of the blade deflection during the rotation may change the peak-to-peak variation of the transient static pressure field. Comparisons in Figs. 9 and 10 show that the pressure wave due to the inlet total pressure distortion travels through the rotor passage. The amplitude and the resulting unsteady aerodynamic loading at high rotor speed are roughly twice those at the low rotor speed.

Effects of Inlet Distortion on Flow Structure. Instantaneous Mach number contours at 85 percent span are plotted to study the unsteady flow fields inside the rotor with inlet distortion. In Fig. 11, instantaneous relative Mach number contours at six equally spaced times during a distortion period are shown. Since the rotor has 16 blades and there are eight distortion patterns per revolution, two blade passages make a nominal periodic cycle.

At this low rotor speed, a passage shock is not expected at 85 percent span. Thus, upstream flow disturbances are not

blocked by shock wave and the inflow distortion affects the entire flow passage almost simultaneously. For both blade passages, a vortex with low Mach number is formed near the pressure side of the blade. The vortex cores (marked as vortices 1 and 2 in Fig. 11) are convected downstream as shown in Figs. 11(a-e). Vortex 2 is convected completely downstream of the blade passage in Fig. 11(f) and a new vortex core is formed. This vortex is convected downstream as the blade moves through the distortion profile. As shown in Fig. 7, the variation of the total pressure across the distortion profile is relatively small at the 68 percent rotor speed. When this distortion pattern reaches the rotor leading edge, a small change in incidence angle is expected. Detailed contours near the leading edge in Fig. 11 show relatively small changes in the flow near the leading edge during the distortion period. Contour lines near the suction surface of the blade show that the boundary layer is almost completely attached during the cycle, although the boundary layer itself is clearly unsteady. The vortex near the pressure surface of the blade is convected downstream, but the thickness of the boundary layer does not increase. The boundary layer on the pressure side of the blade seems to be energized by the unsteady vortex system. Also, flow downstream of the rotor shows more disturbances than the incoming distortion due to the shed vortex. Previous studies of multistage axial compressor aerodynamics have shown that the stage efficiency increases when the axial gap is decreased in some subsonic operating conditions (Smith, 1970; Mikolajczyk, 1977). Smith (1966) suggested a possible explanation of this fascinating phenomenon using the mixing mechanism of an incoming stator wake through the following rotor blade passage. The results in Fig. 11 suggest that there may be other possible mechanisms in reducing aerodynamic losses with narrower gaps between

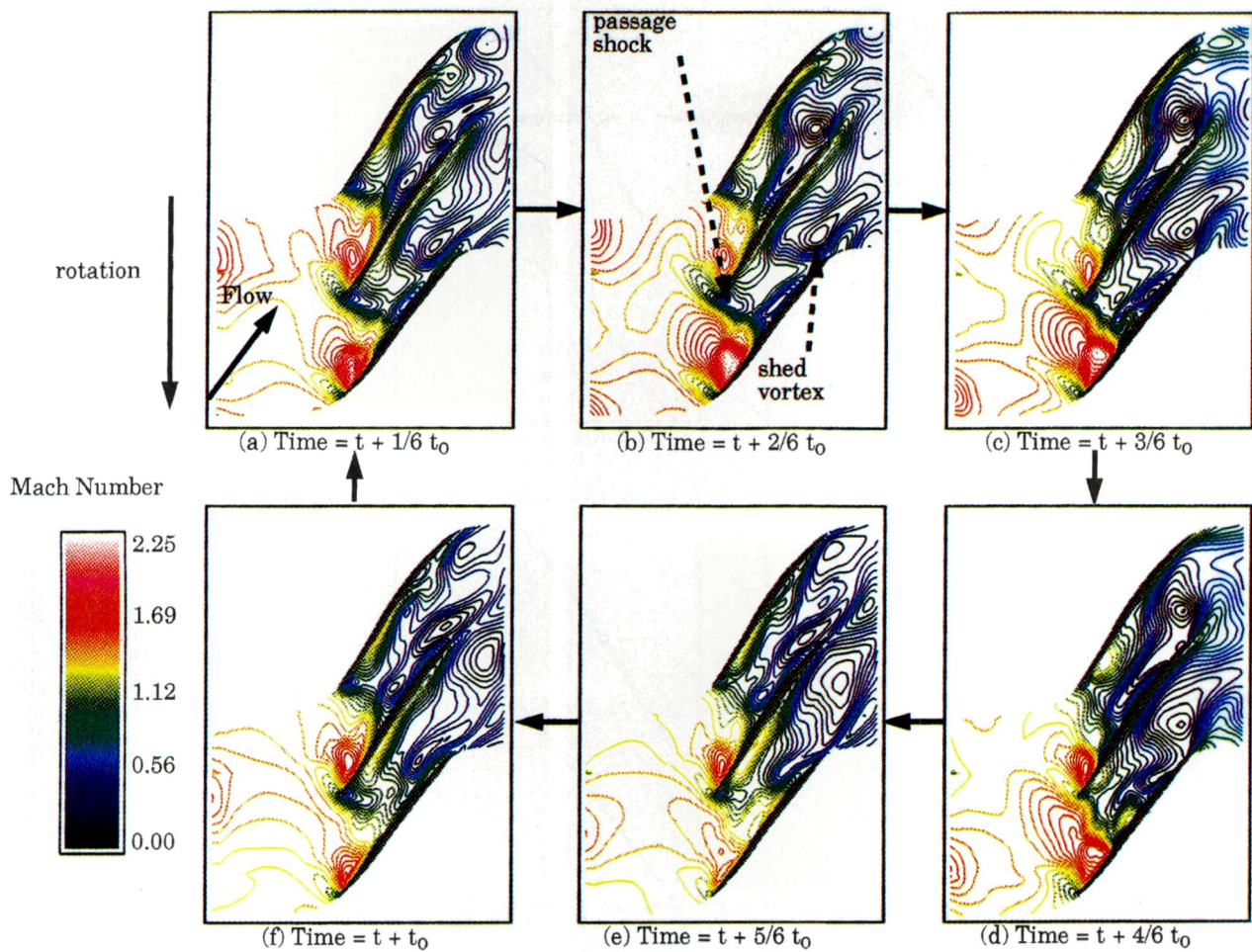


Fig. 13 Instantaneous Mach number contours at 85 percent span for 98 percent rotor speed

blade rows. The detailed flow structures in Fig. 11 suggest that a favorable interaction between the vortex and the blade boundary layer might be one such mechanism.

The instantaneous entropy contours at 5 percent blade chord downstream of the rotor are given in Fig. 12. Regions with high entropy contours represent areas with high aerodynamic losses. A highly fluctuating vortex system (vortex B) is observed in Fig. 12. Entropy generation is confined near the casing and no significant loss is observed in the area of the fluctuating vortex. Further interpretation of the vortex structure in Fig. 12 will be given later in this section with the results at 98 percent rotor speed. The effect of this fluctuating vortex on the rotor performance will be further examined in the next section.

In Fig. 13, instantaneous relative Mach number contours are shown for the 98 percent rotor speed. As shown in Fig. 7, the variation of the total pressure across the distortion pattern is more than 30 percent of the mean value. Therefore, the effects of inlet total pressure distortion on the rotor flow field are expected to be more substantial than at the low rotor speed. At this high rotor speed, a strong passage shock develops near the leading edge of the rotor. The instantaneous Mach number contours in Fig. 13 indicate that the passage shock system oscillates substantially when the rotor blade traverses through the distortion pattern. A strong interaction between the moving shock and the blade boundary layers is observed in Fig. 13. As a result of this strong interaction, large vortices are generated and convected downstream. The formation and convection of a vortex in the blade passage are illustrated in Fig. 14 using constant Mach number contours. During the distortion cycle,

the vortex grows as it is convected downstream within the blade passage. The flow field inside the rotor blade passage is dominated by these vortices. Also, the blade boundary layers grow significantly due to this oscillating shock system. In Fig. 15, the movement of the passage shock during one distortion period is illustrated by the instantaneous sonic line during the cycle. The passage shock moves approximately 20 percent of the chord during the cycle. Ng and Epstein (1985) found for a similar transonic compressor that a very small shock oscillation (about 1 percent of tip chord) can cause an increase of compressor aerodynamic loss of 0.15 percent. A quantitative estimation of the increased loss due to the shock movement in the current rotor will be given in the next section. From the results in Figs. 13, 14, and 15, it is clear that the interaction between the oscillating passage shock and the blade boundary layer, and the resulting vortex shedding shown in Fig. 14, are the dominating flow structures when the transonic compressor encounters a strong circumferentially nonuniform flow distortion.

The instantaneous entropy contours at 5 percent chord downstream of the rotor for 98 percent rotor speed are given in Fig. 16. The time-dependent entropy contours downstream of the rotor at 68 and 98 percent rotor speeds, which are shown in Figs. 12 and 16, respectively, show a complex three-dimensional flow interaction open to several interpretations. Our views on the flow phenomenon calculated by the analysis are summarized as follows.

Two distinct vortex cores labeled vortexes A and B are observed at both 68 and 98 percent rotor speeds as illustrated in Figs. 12 and 16. Vortex A represents the flow field associated

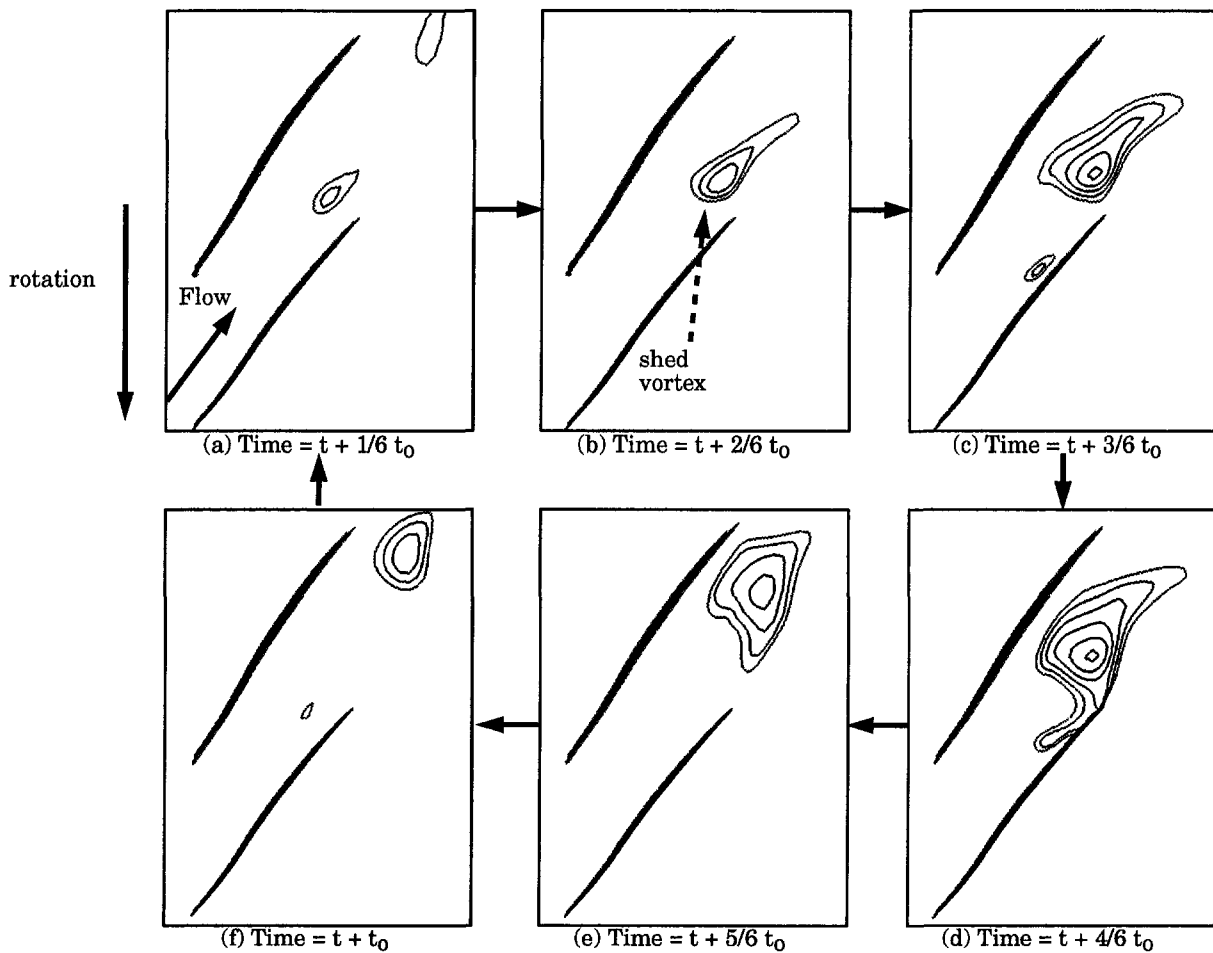


Fig. 14 Formation and convection of a vortex at 85 percent span for 98 percent rotor speed

with the tip shock and the clearance flow and vortex B is related to the secondary flow being centrifuged radially outward along the suction surface of the airfoil.

The core of vortex A, shown in Fig. 12, is circumferentially located approximately 40 percent of the distance from the airfoil pressure surface to the adjacent suction surface, and extends about 20 percent span inward from the casing wall. At higher relative velocities (98 percent speed), the interaction between the tip clearance vortex and the relatively stronger leading edge shock is larger and vortex A extends deeper to about 40 percent span inward from the casing endwall as shown in Fig. 16. The unsteady motion of the vortex A, attributed in part to the shock oscillation (typically illustrated in Fig. 15), is shown at selected time steps in Figs. 12(a-d) for 68 percent speed and Figs. 16(a-d) for 98 percent speed. At both speeds, the core of vortex A relocates from midpassage ($t + t_o/4$) to the pressure side of the airfoil ($t + 2t_o/4$). The core moves back to midpassage as the solution progresses to the next time step ($t + 3t_o/4$ in Figs. 12 and 16). As stated above, the motion of vortex A is supported by the shock oscillation reported in Fig. 15.

The secondary flow vortex (vortex B) forms a vortex core near the casing at $t + t_o/4$ as shown in Figs. 12 and 16 and migrates from the suction side toward the pressure side of the airfoil as the numerical calculations progress in time from $t + t_o/4$ and $t + 3t_o/4$ to $t + t_o$ as shown in Figs. 12(b-d). Little interaction between the secondary flow and the clearance vortex occurs at 68 percent speed; vortices A and B maintain their identities as they migrate with time. However, at 98 percent speed, the effect of the secondary flow vortex is considerably

masked by the stronger and more dominant tip clearance vortex flow, as shown in Figs. 16(a-d).

Effects of Inlet Distortion on Compressor Performance. To compare the overall effects of inlet total pressure distortion on the performance of the rotor, spanwise distributions of blade section efficiency are compared between the clean inlet flow and the flow with the distortion. In Fig. 17, comparisons at 68 percent of the rotor design speed are presented. The measured distributions and the calculated distributions are compared. The calculated profiles are obtained by averaging instantaneous profiles over the distortion period. According to the measured distributions, the blade section efficiency improves above 70 percent of the blade span for the presently investigated distortion compared to the clean inlet case. The calculation shows the same changes as the measurements. Because of the increased blade section efficiency near the shroud, the overall blade efficiency increases by 0.4 percent with distortion. At this flow condition, the distortion does not change the blade section efficiency near the hub as shown in Fig. 17. To examine the flow behavior further, the instantaneous entropy contours at 85 percent span are averaged and compared with the steady results for the clean inlet condition in Fig. 18. This comparison indicates that the time-averaged unsteady flow field with the distortion shows no noticeable increase in boundary layer growth compared to the clean inlet case. The results shown in Fig. 17 indicate that the vortex generated inside the passage (as shown in Fig. 11) does not contribute to added overall loss. The smaller generation of entropy in Fig. 18 for the flow with inlet distortion suggests

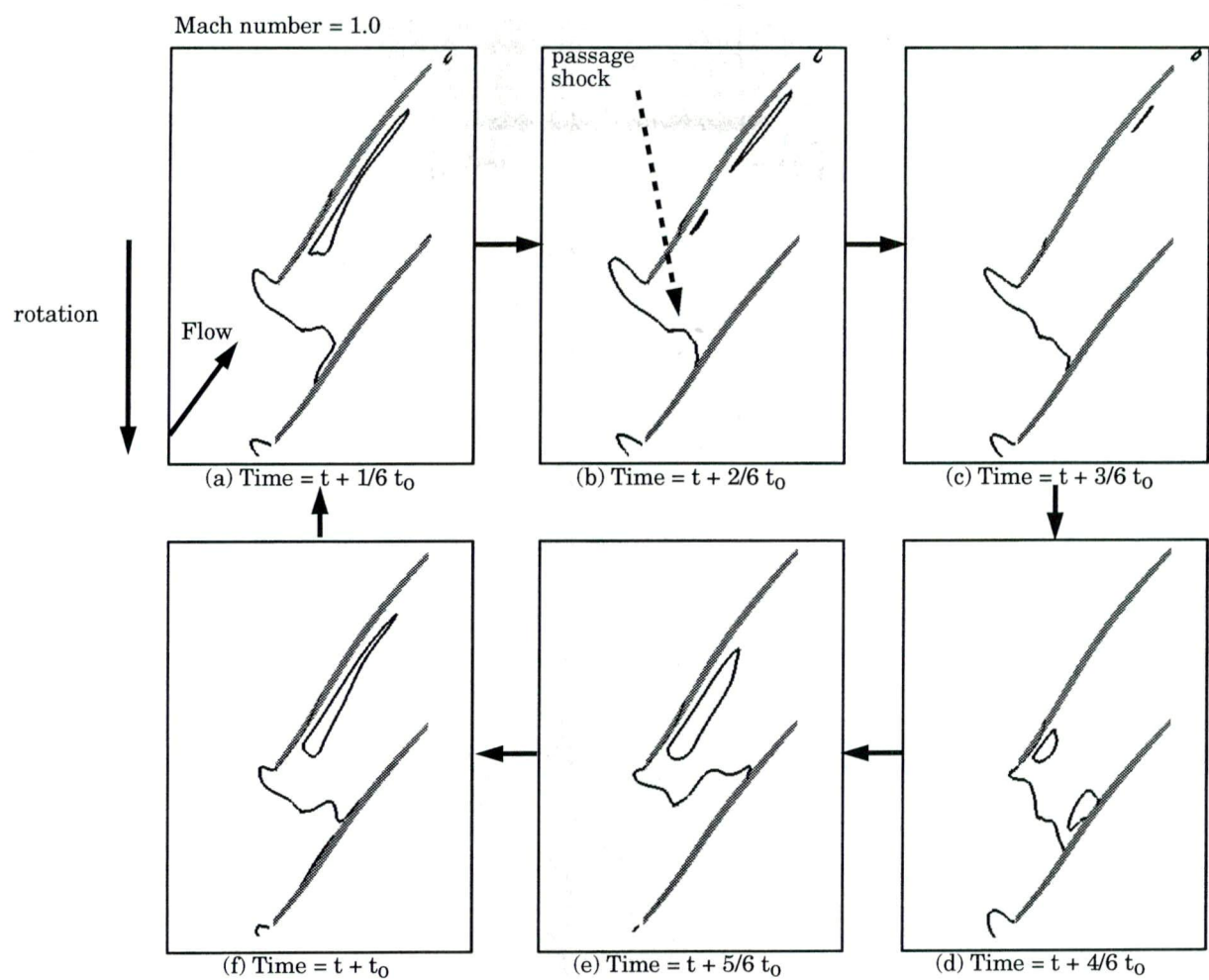


Fig. 15 Movement of passage shock over one distortion period at 85 percent span for 98 percent rotor speed

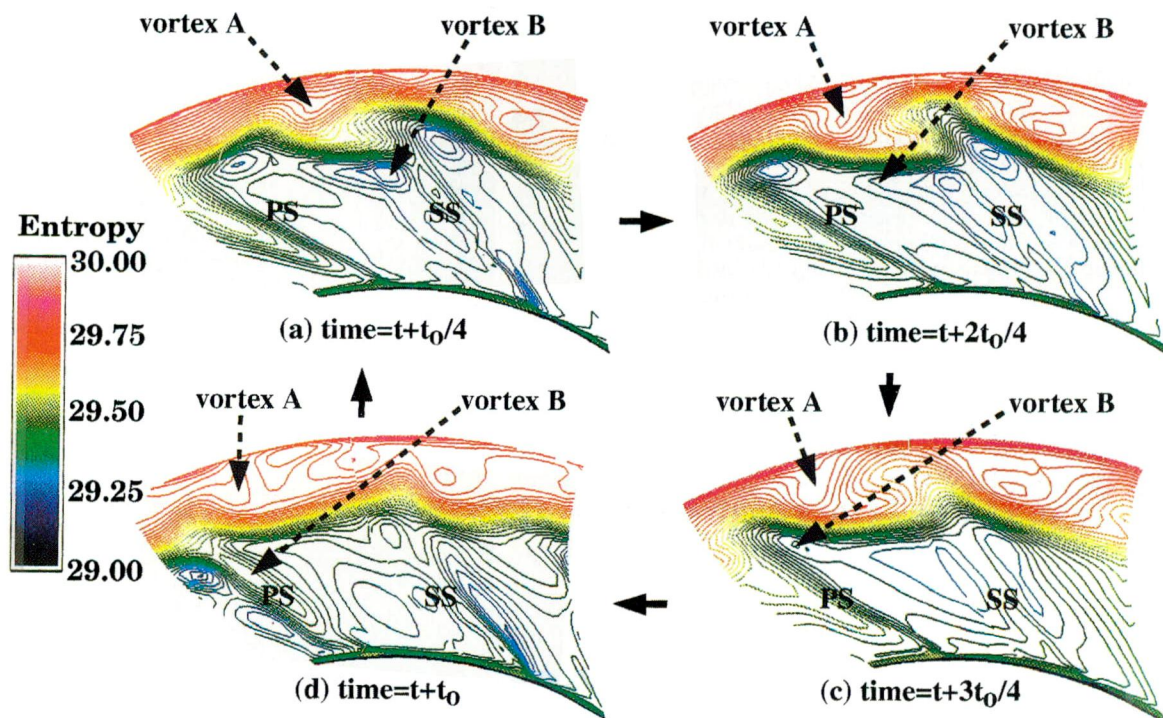


Fig. 16 Instantaneous entropy contours at 5 percent chord downstream of trailing edge for 98 percent rotor speed

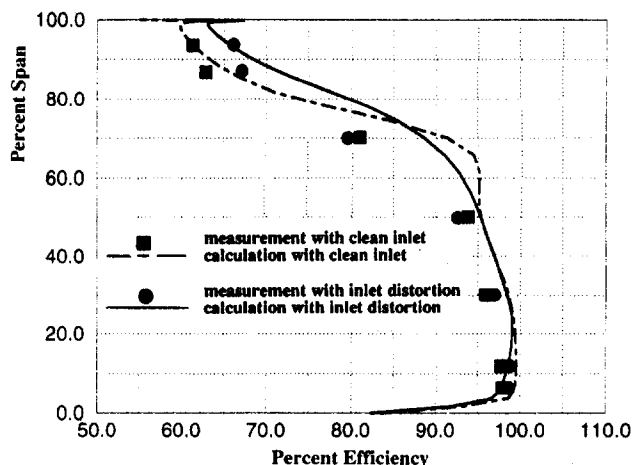


Fig. 17 Comparison of blade section efficiency at 68 percent rotor speed

that the flow near the blade surface is energized by the shed vortex.

As shown in Fig. 13, the effective blockage inside the blade passage increases with the inlet distortion, resulting in an increased blade loading. To obtain a more realistic assessment of the effects of distortion, an additional rotor flow field without distortion at a high pressure ratio is also compared. This operating condition is marked in Fig. 5. The shock structures at two operating conditions are compared with the time-averaged unsteady solution with the inlet distortion in Fig. 19. The blade section efficiencies are compared in Fig. 20 for the 98 percent rotor design speed. At this high speed, the spanwise distribution of loss is quite different from that at low speed. The measurements show that the blade section efficiency is higher with the inlet distortion below 60 percent of the span while the efficiency is somewhat lower above 60 percent of the span when compared to the efficiency with clean inlet. The numerical results show the same trend for the effects of inlet distortion on blade section efficiency as the measurements. As shown in Fig. 19, the rotor operates at a higher loading with the inlet distortion. Therefore, the blade section efficiency with the inlet flow distortion should be compared with the clean inlet flow, which has a similar loading distribution. As shown in Fig. 20, the blade section efficiency with the distortion is lower than that of the flow with the clean inlet and a similar shock structure near the end wall. This decrease in the blade section efficiency is due to the strong interaction between the oscillating passage shock and the blade boundary layer that is shown in Fig. 13. Because the mass flow rate is higher near the shroud, the overall rotor efficiency decreases with the inlet distortion. The calculated decrease is 1 percent with the inlet total pressure distortion. Time-averaged instantaneous entropy contours at 85 percent span are compared with the steady results in Fig. 21. This comparison indicates that the large entropy generation is concentrated near the suction side of the blade for the flow with the distortion. This again indicates that unsteady interaction between the passage shock and the suction surface boundary layer is the major contributor to the aerodynamic loss when a transonic rotor flow field is subjected to a strong inlet total pressure distortion.

Concluding Remarks

The effects of inlet total pressure distortion on the flow field in a low-aspect-ratio, high-speed, transonic compressor rotor have been investigated. Both experimental and numerical techniques are applied in a complementary way to ad-

vance our present understanding of this very complex flow field. The following is a summary of the current study:

1 The inlet flow distortion travels through the rotor passage and is convected into the following stator. The highly transient flow field is observed at both low and high rotor speeds with the inlet flow distortion.

2 At 68 percent rotor design speed, both the measurement and the calculation show that the blade section efficiency with the inlet distortion is higher than that with clean inlet flow above 70 percent of the span. The numerical results indicate that the increased blade section efficiency in the outer region of the rotor blade might be the result of favorable effects of the interaction between the passage vortices and the blade boundary layer.

3 At 98.6 percent rotor design speed, a strong interaction between the oscillating passage shock and the blade suction surface boundary layer increases the effective blockage and forces the rotor to operate closer to the stall condition. When compared to a clean inlet flow field with a similar loading, inlet total pressure distortion decreases the blade section efficiency above 60 percent of the blade span. However, improvements in blade section efficiency are observed near the hub when com-

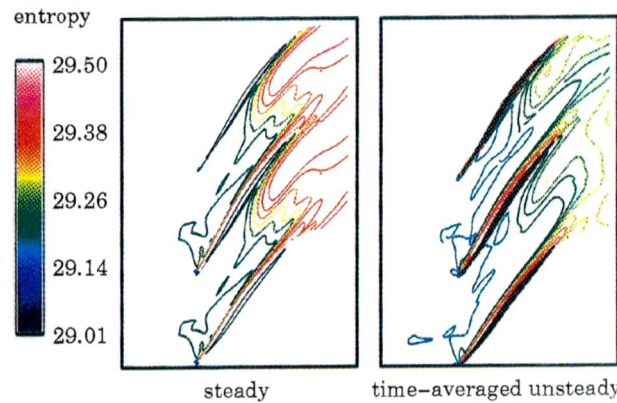


Fig. 18(a) Comparison of entropy contours at 85 percent span for 68 percent rotor speed

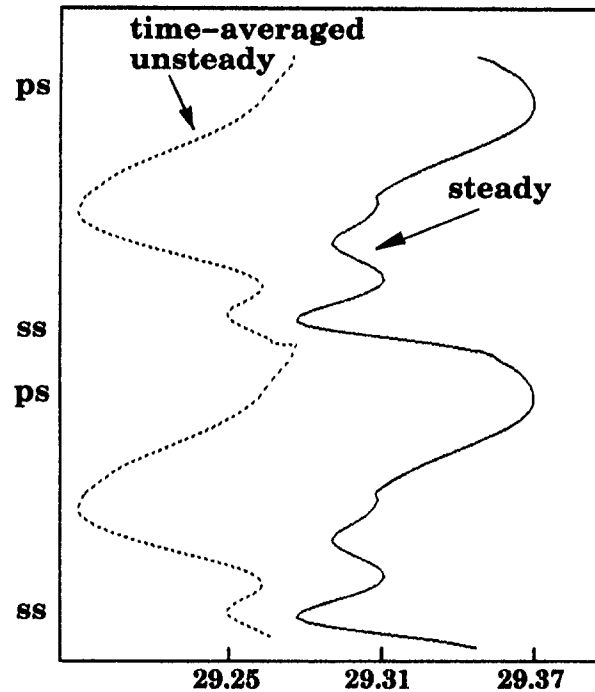


Fig. 18(b) Comparison of entropy distribution at 20 percent chord downstream and 85 percent span for 68 percent rotor speed

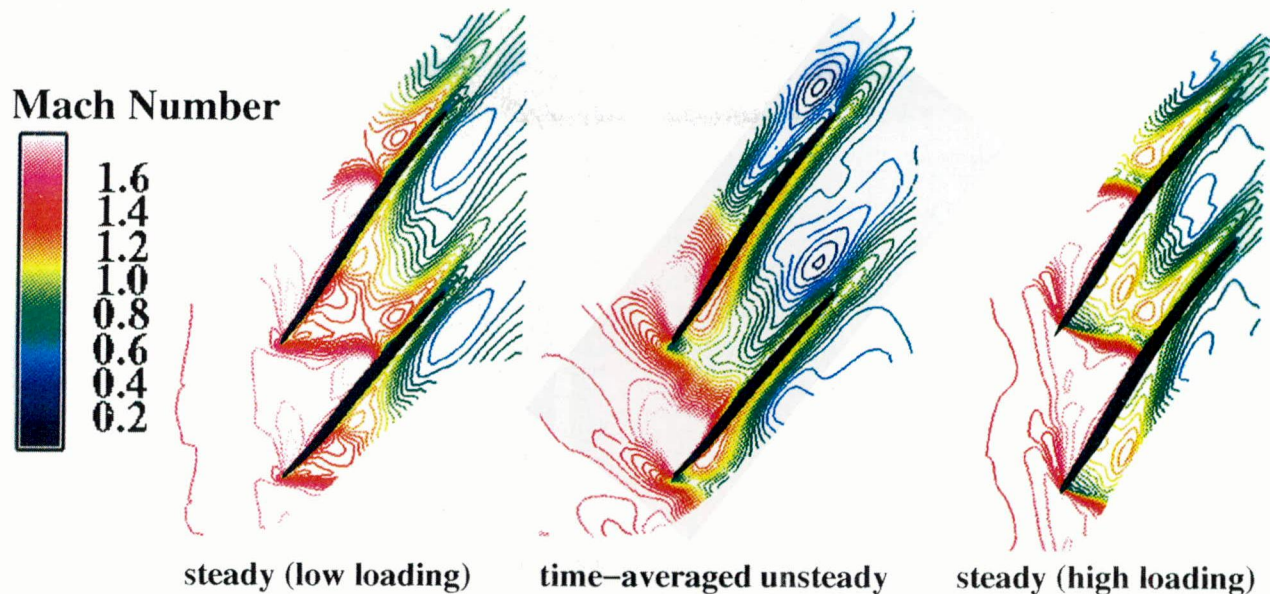


Fig. 19 Comparison of relative Mach number contours at 85 percent span for 98 percent rotor speed

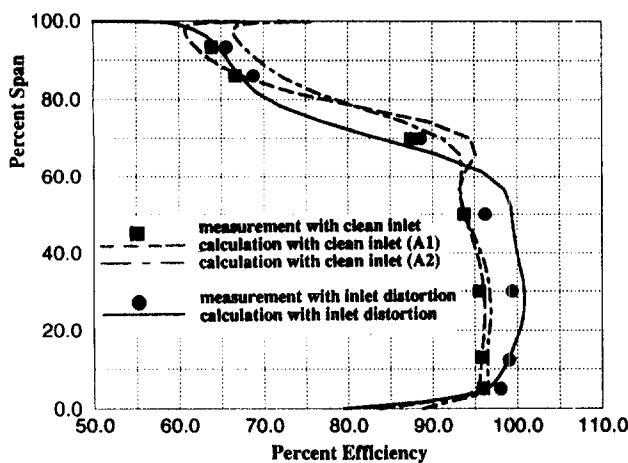


Fig. 20 Comparison of blade section efficiency at 98 percent rotor speed

pared to the clean rotor flow field. The numerical results show that the increased loss in the outer part of the blade is due to the strong interaction between the oscillating passage shock and the blade boundary layer. A vortex shedding occurs due to this interaction. The passage shock moves by as much as 20 percent of the chord during the distortion period. The blade boundary layer thickens substantially due to the unsteady interaction with the passage shock.

4 The current study indicates that the inlet total pressure distortion increases aerodynamic losses when a strong unsteady interaction between the passage shock and the blade boundary layer develops. However, a subsonic flow range exists in which the inlet total pressure distortion can actually improve the rotor performance.

Acknowledgments

The authors would like to acknowledge the contribution of J. Loellbach and F. Tsung of ICOMP at NASA Lewis Research Center in preparing the illustrations. Also, we would like to thank G. E. Aircraft Engine Company, Wright Laboratory, and NASA for allowing us to present this work.

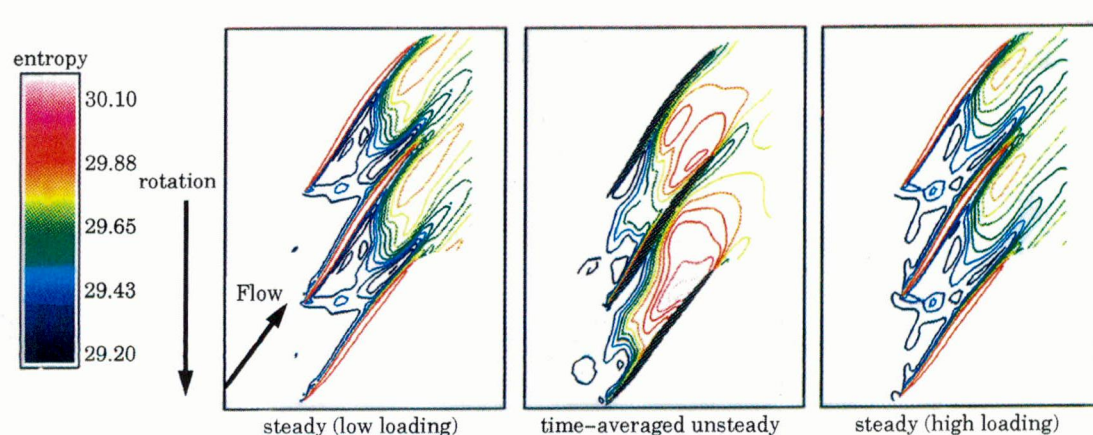


Fig. 21 Comparison of entropy contours at 85 percent span for 98 percent rotor speed

References

- Adamczyk, J. J., Mulac, R. A., and Celestina, M. L., 1986, "A Model for Closing the Inviscid Form of the Average Passage Equations," *ASME JOURNAL OF TURBOMACHINERY*, Vol. 108, pp. 180–186.
- Bowditch, D. N., and Coltrin, R. E., 1983, "A Survey of Engine Inlet Distortion Capability," NASA TM-83421.
- Cho, N.-H., Liu, X., Rodi, W., and Schonung, B., 1993, "Calculation of Wake-Induced Unsteady Flow in a Turbine Cascade," *ASME JOURNAL OF TURBOMACHINERY*, Vol. 115, pp. 675–686.
- Copenhaver, W. W., Hah, C., and Puterbaugh, S. L., 1993, "Three-Dimensional Flow Phenomena in a Transonic, High-Through-Flow Compressor Stage," *ASME JOURNAL OF TURBOMACHINERY*, Vol. 115, pp. 240–248.
- Davis, R. L., Hobbs, D. E., and Weingold, H. D., 1988, "Prediction of Compressor Cascade Performance Using a Navier–Stokes Technique," *ASME JOURNAL OF TURBOMACHINERY*, Vol. 110, pp. 520–531.
- Dawes, W. N., 1986, "Development of a 3D Navier–Stokes Solver for Application to All Types of Turbomachinery," ASME Paper No. 86-GT-70.
- Denton, J. D., and Singh, U. K., 1979, "Time Marching Methods for Turbomachinery Flow Calculation," VKI Lecture Series, 1979–7.
- Denton, J. D., 1986, "The Use of a Distributed Body Force to Simulate Viscous Flow in 3D Flow Calculations," ASME Paper No. 86-GT-144.
- Gallus, H. E., Zeschky, J., and Hah, C., 1995, "Endwall and Unsteady Flow Phenomena in an Axial Turbine Stage," *ASME JOURNAL OF TURBOMACHINERY*, Vol. 117, pp. 562–570.
- Giles, M. B., 1988, "Stator/Rotor Interaction in a Transonic Turbine," *AIAA Paper No. 88-3093*.
- Greitzer, E. M., Tan, C. S., Wisler, D. C., Adamczyk, J. A., and Strazisar, A. J., 1994, "Unsteady Flow in Turbomachines: Where's the Beef?" *ASME AD-Vol. 40*, Ng, W., Fant, D., and Povinelli, L., eds.
- Gundy-Burlet, K. L., Rai, M. M., Stauffer, R. C., and Dring, R. P., 1991, "Temporally and Spatially Resolved Flow in a Two-Stage Axial Compressor: Part 2—Computational Assessment," *ASME JOURNAL OF TURBOMACHINERY*, Vol. 113, pp. 227–232.
- Hah, C., 1984, "A Navier–Stokes Analysis of Three-Dimensional Turbine Flows Inside Turbine Blade Rows at Design and Off-Design Conditions," *ASME Journal of Engineering for Gas Turbines and Power*, Vol. 106, pp. 421–429.
- Hah, C., 1987, "Calculation of Three-Dimensional Viscous Flows in Turbomachinery With an Implicit Relaxation Method," *AIAA Journal of Propulsion and Power*, Vol. 3, No. 5, pp. 415–422.
- Hah, C., and Wennerstrom, A. J., 1990, "Three-Dimensional Flowfields Inside a Transonic Compressor With Swept Blades," *ASME JOURNAL OF TURBOMACHINERY*, Vol. 113, pp. 241–251.
- Hah, C., Puterbaugh, S. L., and Copenhaver, W. W., 1993, "Unsteady Aerodynamic Flow Phenomena in a Transonic Compressor Stage," *AIAA Paper No. 93-1868*; to be printed in the *AIAA Journal of Propulsion and Power*.
- Hall, E. J., Heidegger, N. J., and Delaney, R. A., 1996, "Performance Prediction of Endwall Treated Fan Rotors With Inlet Distortion," *AIAA Paper No. 96-0244*.
- Horlock, J. H., 1968, "Fluctuating Lift Forces on Airfoils Moving Through Transverse and Chordwise Gusts," *ASME Journal of Basic Engineering*, Vol. 90, Paper No. 68-FE-28.
- Jorgenson, P. C. E., and Chima, R. V., 1988, "An Explicit Runge–Kutta Method for Unsteady Rotor/Stator Interaction," *AIAA Paper No. 88-0049*.
- Longley, J. P., 1988, "Inlet Distortion and Compressor Stability," Ph.D. Dissertation, Cambridge University.
- Mikolajczak, A. A., 1977, "The Practical Importance of Unsteady Flow," AGARD CP-177, *Unsteady Phenomena in Turbomachinery*.
- Monsarrat, N. T., 1969, "Design Report: Single-Stage Evaluation of Highly-Loaded High-Mach-Number Compressor Stages," NASA CR 72562.
- Moore, J., and Moore, J. E., 1981, "Calculations of Three-Dimensional Viscous Flow and Wake Development in a Centrifugal Impeller," *ASME Journal of Engineering for Power*, Vol. 103, pp. 367–372.
- Ng, W. F., and Epstein, A. H., 1985, "Unsteady Losses in Transonic Compressors," *ASME Journal of Engineering for Gas Turbines and Power*, Vol. 107, pp. 345–353.
- Ni, R. H., and Bogoian, J. C., 1989, "Prediction of 3D Multi Stage Turbine Flow Field Using a Multiple Grid Euler Solver," *AIAA Paper No. 89-0203*.
- Rabe, D., Bolcs, A., and Russler, P., 1995, "Influence of Inlet Distortion on Transonic Compressor Blade Loading," *AIAA Paper No. 95-2461*.
- Rai, M. M., 1985, "Navier–Stokes Simulations of Rotor–Stator Interaction Using Patched and Overlaid Grids," *AIAA Paper No. 85-1519*.
- Rao, K., and Delaney, R., 1990, "Investigation of Unsteady Flow Through Transonic Turbine Stage," *AIAA Paper No. 90-2408*.
- Russler P. M., 1994, "Acquisition and Reduction of Blade-Mounted Pressure Transducer Data From a Low Aspect Ratio Fan," WR-TR-94-2021.
- Russler, P. M., 1995, "Acquisition and Reduction of Rotor Tip Static Pressure Transducer Data From a Low Aspect Ratio Transonic Fan," WR-TR-95-2022.
- Smith, L. H., 1966, "Wake Dispersion in Turbomachines," *ASME Journal of Basic Engineering*, Vol. 88, pp. 688–690.
- Smith, L. H., 1970, "Casing Boundary Layers in Multistage Axial Flow Compressors," in: *Flow Research on Blading*, L. S. Dzung, ed., Elsevier Publishing Company, Amsterdam, No. 3, pp. 688–690.
- Wennerstrom, A. J., 1984, "Experimental Study of a High-Through-Flow Transonic Axial Compressor Stage," *ASME Journal of Engineering for Gas Turbines and Power*, Vol. 106, pp. 552–560.